Hydrodynamic Porosity:
A Paradigm Shift in Flow and Contaminant Transport Through Porous Media, Part II

August H. Young[1,2], Zbigniew J. Kabala[3]

5 [1] Duke Center for WaSH-AID, Durham, NC, 27701, USA
   [2] Mechanical Engineering and Materials Science, Duke University, Durham, NC, 27710, USA
   [3] Civil and Environmental Engineering, Duke University, Durham, NC, 27710, USA

Correspondence to: August H. Young (ahf12@duke.edu)

Abstract

10 In this work, we build upon our previous finding that hydrodynamic porosity, θ_{mobile}, is an exponential function of pore-scale flow velocity (or interstitial Reynolds number). We previously discovered this relationship for media with a square cavity geometry – a highly idealized case of the dead-ended pore spaces in a porous medium. Thus, we demonstrate the applicability of this relationship to media with other cavity geometries. We do so by applying our previous analysis to rectangular and non-rectangular cavity geometries (i.e., circular, and triangular). We also study periodic flow geometries to determine the effect of

15 upstream cavities on those downstream. We show that not only does our exponential relationship hold for media with a variety of cavity geometries, but it does so almost perfectly with a coefficient of determination (R^2) of approximately 1 for each new set of simulation data. Given this high fit quality, it is evident that the exponential relationship we previously discovered is applicable to most, if not all, unwashed media.

Keywords: *Hydrodynamic Porosity, Cavity, Dead-End Pore, Pore Velocity, Volumetric Velocity, Reynolds Number,*
20 *Groundwater Remediation*

1 Introduction

In this paper, we build on our previous findings, i.e., Young and Kabala (2023), where we discovered and quantified the exponential dependence of hydrodynamic porosity (θ_{mobile}) on pore-scale flow velocity (v_{pore}) or interstitial Reynolds Number (Re). This relationship is reproduced below:

25
$$\theta_{mobile} = (a + be^{-c\,v_{pore}})\,\theta \iff \theta_{mobile} = (a + be^{-d\,Re})\,\theta, \qquad d = \frac{c\ height}{\nu} \qquad (1)$$

Where θ_{mobile} is the mobile-zone porosity (what we refer to as the hydrodynamic porosity of the medium), θ is the total porosity of the medium (i.e., V_{pore}/V_{bulk}), $height$ is the height of the through-channel in the dead-end pore model (m), ν is

the kinematic viscosity (m²/s), and *a, b,* and *c* are dimensionless parameters; the exponential parameter, *d* has units of (s/m) to allow for use of pore-scale velocity in place of Reynolds number. Readers are further reminded that *a* is the value of the pore-

30 scale partitioning coefficient (ξ) approximated by the boundary-driven, or analogously, Mobile-Immobile Zone model, both of which are discussed at length by Young and Kabala (2023), and originally applied to groundwater flows by Vangenuchten and Wierenga (1976). In the case of the mobile separatrix we study here, it is the value that results from $Re \to \infty$. Finally, the quantity '*a + b,*' is the value of ξ in the creeping flow regime (i.e., the value that results from $Re \to 0$).

35 Equation (1) was discovered and quantified for the dead-end pore geometry reproduced in Figure 1, below. Readers will note that the cavity geometry is square. *Thus, we did not previously determine if this relationship holds for more than this single idealized case.* This work is motivated by the fact that the dead-ended pore spaces in unwashed porous media (e.g., glacial deposits, fractured rock, and filtration media such as granulated activated carbon, etc.) are poorly approximated by the square cavity geometry we previously studied. The jagged edges of such media result in a random array of pore geometries (as

40 illustrated below). Subsequently, we must be able to answer the question: does the exponential dependence of hydrodynamic porosity, θ_{mobile}, on pore-scale flow velocity hold for media with cavity geometries that are not square? If the answer is indeed *yes*, researchers are justified in utilizing the exponential relationship provided in Eq. (1). Further, researchers can expand upon this relationship by determining if θ_{mobile} exhibits a dependence on any other aspects of the dead-end pore geometry (e.g., depth, width, hydraulic radius, etc.).
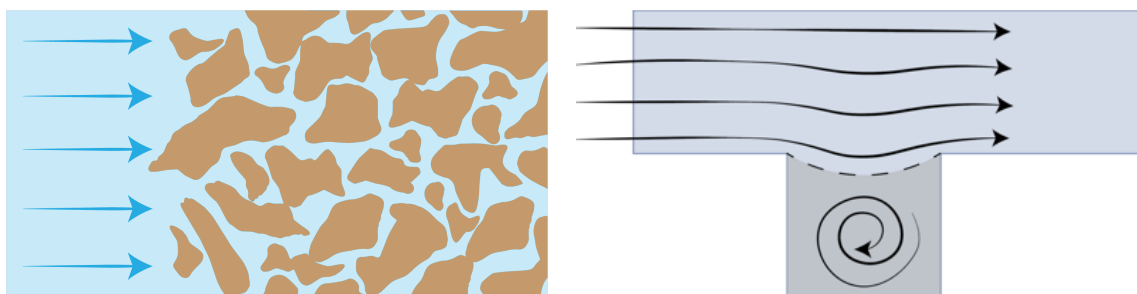
45 **Figure 1: Illustration of the pore space and cavities in an unwashed porous media and the idealized dead-end pore geometry used by Young and Kabala (2023) (left and right, respectively).**

2 Related Work

2.1 Flows Past Cavities

In our previous work, we provide a thorough literature review of flows past cavities, citing the major contributions that have

50 led to a comprehensive understanding of cavity vortex structure(s) (Moffatt, 1963; Higdon, 1985; Shen and Floryan, 1985; Fang et al., 1997). Readers are directed to this discussion for further detail. In the following table, we summarize the popular

cavity geometries studied by these (and other) authors. Following the precedent set by these authors, we proceed by utilizing the same cavity geometries in our analysis.

Table 1: Geometries used in the study of flows past cavities.

Cavity Geometry		
Rectangular	Non-Rectangular	Periodic
• Young and Kabala (2023) • Kahler and Kabala (2016) • Moffatt (1963) • Mehta and Lavan (1969) • O' Brien (1972) • Shen and Floryan (1985) • Kang and Chang (1982) • Fang et al. (1997) • Higdon (1985) • Alkire et al. (1990) • Horner et al. (2002)	• Moffatt (1963) • Higdon (1985) • O'neill (1977)	• Kahler and Kabala (2016) • Kang and Chang (1982)

55

Table 1 illustrates that most research has been carried out on rectangular cavity geometries. This is unsurprising given that sharp corners in flow geometries result in flow separation. Mehta and Lavan (1969), O' Brien (1972), Shen and Floryan (1985), Fang et al. (1997), and Higdon (1985) utilize rectangular geometries and manipulate the cavity width and/or depth to determine the subsequent effect on the cavity vortex structure. Moffatt (1963), in his study on resistive eddies that result from sharp

60 corners, focuses most of his work on triangular structures, while Higdon (1985) and O'neill (1977) study circular cavities.

2.2 Our Previous Work

The idealized, square cavity geometry we previously utilized in Young and Kabala (2023) is justified by its foundational use in the study of flows past cavities, as noted by Shankar and Deshpande (2000) and is included in most of the studies referenced in Table 1 above. To exaggerate the dependence of hydrodynamic porosity, θ_{mobile}, on pore velocity, we also narrowed the

65 height of the through-channel, relative to the cavity depth and width, which is kept at a one-to-one aspect ratio so that the cavity remains square; readers are referred to Figure 6 of Young and Kabala (2023) for reference.

We then subjected these dead-end pore geometries to inlet flows with an interstitial (channel-based) Reynolds number in the range of 1–100, reasoning that doing so keeps the flow within the laminar regime. To justify this claim, we reference multiple

70 examples that demonstrate a general trend: the onset of turbulence occurs at or above Reynolds numbers of 100 in porous media (Jolls and Hanratty, 1966; Wegner et al., 1971; Latifi et al., 1989; Rode et al., 1994; Bu et al., 2014). For each dead-end pore geometry, we discovered an exponential dependence of hydrodynamic porosity, θ_{mobile}, on pore-scale flow velocity, with a coefficient of determination (R^2) of approximately 1 for each set of simulation data. As anticipated, this relationship was most exaggerated when the through-channel height of the dead-end pore geometry was reduced to one-quarter of the

75 cavity depth/width. For media with this cavity type, θ_{mobile} decreased by 42% over the laminar flow regime. For reference, over the same Reynolds number range, θ_{mobile} only decreased by 4% when the through-channel height was equivalent to the cavity depth/width.

3 Methods

In short, the hydrodynamic porosity, θ_{mobile}, of a porous medium with dead-ended pore spaces is ultimately determined by

80 the location of the separatrix (i.e., the streamline that divides the through-channel flow from the recirculatory cavity flow), which we track over a range of flow conditions by varying the magnitude of the interstitial Reynolds number of the inlet flow. Further discussion on the separatrix is provided by Elderkin (1975), Weiss (1991), Horner et al. (2002), and Kahler and Kabala (2016). We track the location of the separatrix because it defines the magnitude of the mobile zone (i.e., the pore space conducive to through-flow), and therefore the value of the pore-space partitioning coefficient, ξ:

85
$$\xi \ = \ \frac{V_{mobile}}{V_{pore}} = \frac{A_{mobile}}{A_{pore}} \tag{2}$$

As defined above, ξ is the ratio of the mobile-zone volume (V_{mobile}) to the total pore space volume (V_{pore}). For an isotropic, or 2D media, like the ones we study in this work, ξ can be defined in terms of cross-sectional areas, A. To relate ξ to θ_{mobile}, we remind readers of the definition of θ, the total porosity:

$$\theta \ = \ \frac{V_{pore}}{V_{bulk}} \tag{3}$$

90 Similarly, θ_{mobile} is defined as:

$$\theta_{mobile} \ = \ \frac{V_{mobile}}{V_{bulk}} \tag{4}$$

Combining Eq. (2) – (4), we find that the product of the total porosity of the medium and the partitioning coefficient yield the hydrodynamic porosity, θ_{mobile}, of the medium:

$$\theta_{mobile} = \ \xi \, \theta \tag{5}$$

95 The methods and tools used in this analysis are the same as those used in our previous work. Readers are directed to Young and Kabala (2023) for a description of the numerical flow solver we leverage in this analysis, as well as a detailed outline of the data collection process. Slight modifications to the flow solver program allow for manipulation of the cavity geometry, which we picture in the figures below. With each cavity manipulation, we adjust the refinement region of the solver mesh to fully encapsulate the area in which we assume the separatrix to be. Altogether, we test rectangular cavities with depth-to-width

100 ratios of 2:1, 1.5:1, 1:1, and 0.5:1 (pictured in Figure 2), and 1:2, 1:1.5, 1:1, and 1:0.5 (pictured in Figure 3). The varying channel length in the geometries provided in Figure 3 is an artifact of the decision to extend the length of the through-channel

past the cavity by twice the cavity width. We also test two non-rectangular cavities (i.e., a semicircle and an equilateral triangle). Finally, we test a periodic flow geometry to determine the effect upstream cavities have on those downstream. These additional flow geometries are provided below, in Figures 4 and 5.
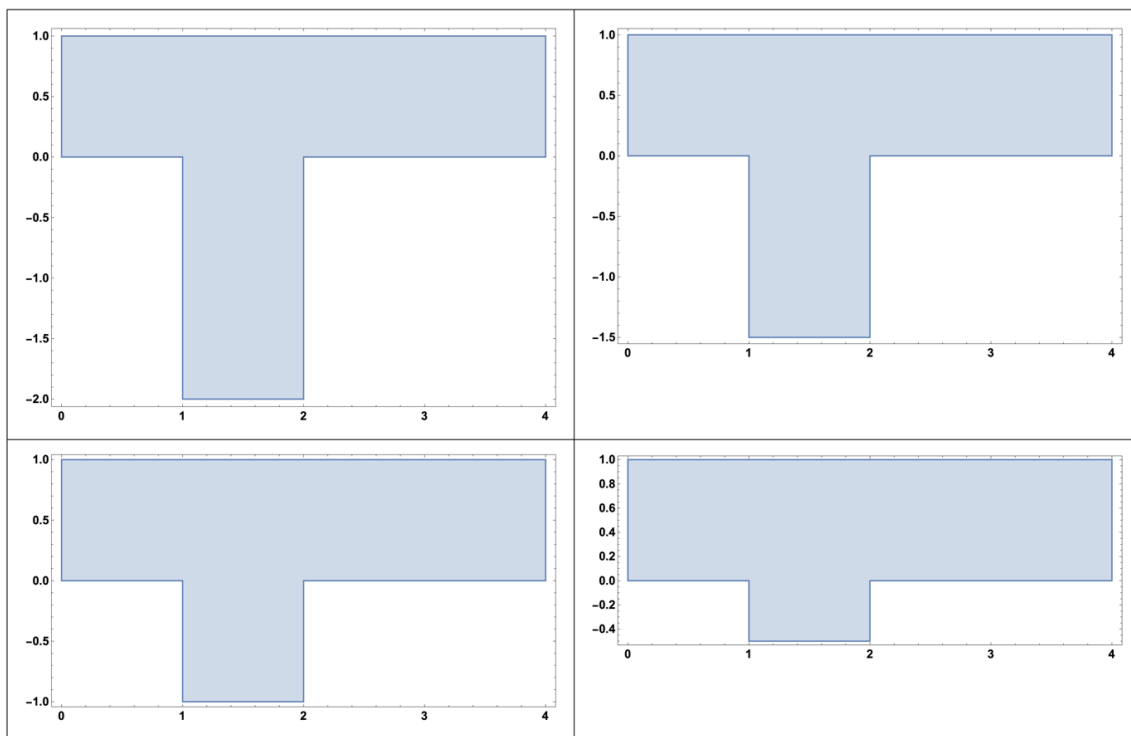
105

Figure 2: Flow geometries with a cavity depth-to-width ratio of 2:1, 1.5:1, 1:1, and 0.5:1 (left to right, top to bottom).
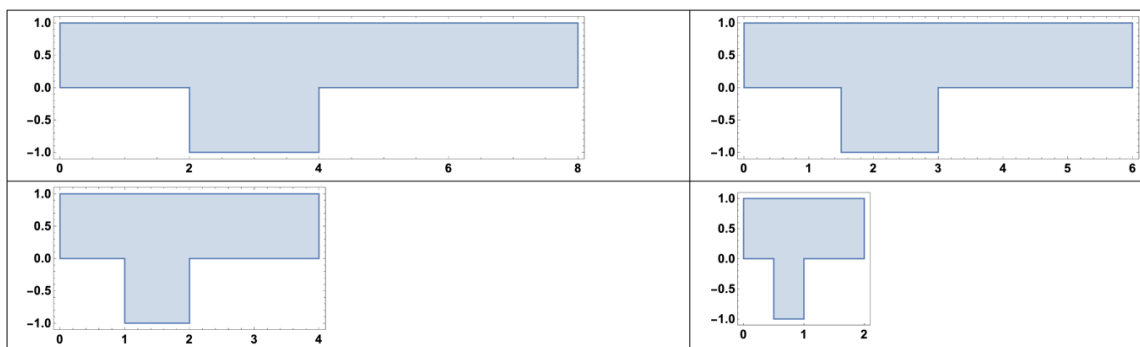
Figure 3: Flow geometries with a cavity heigh-to-width ratio of 1:2, 1:1.5, 1:1, and 1:0.5 (left to right, top to bottom).
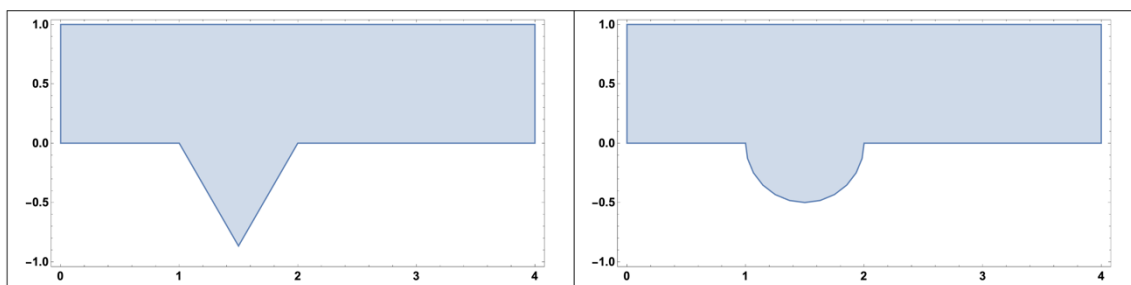
Figure 4: Triangle and circular cavity geometries.
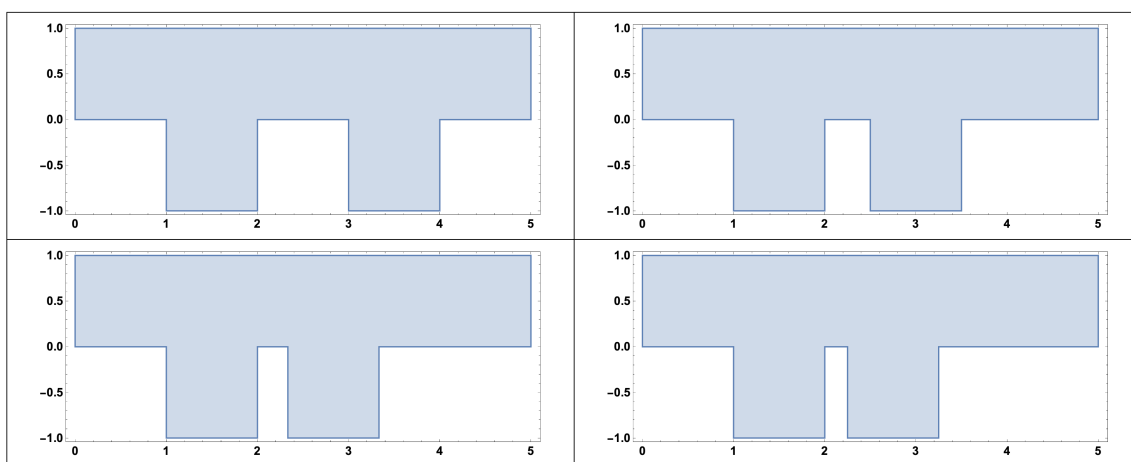
Figure 5: Periodic flow geometries with square cavities. The spacing between the cavities is a fraction of the cavity depth/width (i.e., from left to right, top to bottom: 1, 0.5, 0.33, 0.25).

Again, these flow geometries are subjected to an inlet flow with channel-based Reynolds numbers in the laminar flow regime (i.e., $Re < 100$). For ease of comparison to our previous results, we determine the location of the separatrix at the same Reynolds numbers (i.e., $Re = 1.81, 3.61, 5.52, 9.19, 25, 50, 75, 100$). Note that we do not test Reynolds numbers in the creeping flow regime, which in this case, is less than 1. This is because we previously found that the separatrix is immobile in this regime (Young and Kabala, 2023). After having subjected each flow geometry to the specified Reynolds numbers, we apply the exponential relationship in Eq. (1) that we discovered for the square cavity geometry to each new set of simulation data. We determine the fit quality of the exponential model via the coefficient of determination (R^2). Finally, given the sparse sampling we previously used to generate the exponential relationship we define in Eq. (1), we also determine the error associated with this low sampling frequency; we do this by testing Reynolds numbers of 1–100 in increments of 5.

4 Results

Stream plots for each cavity geometry at Reynolds numbers of approximately 1, 10, 50, and 100, are provided in the figures below. In each stream plot, the separatrix is highlighted in red. Again, because the cavity flow is driven by the adjacent through-

channel flow, we also provide a stream plot of the entire dead-end pore geometry adjacent to the corresponding cavity flow. Figure 6 is reproduced from our previous work.
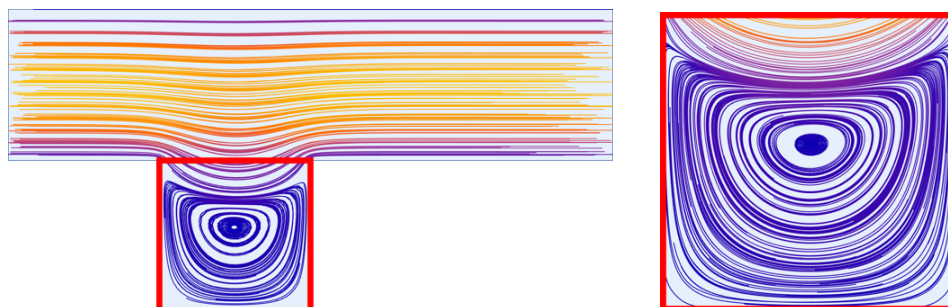
Figure 6: Stream plot magnification example.

130 4.1 Separatrix Movement: Rectangular Cavity Geometry Manipulation

In Figure 7 and 8, we provide the stream plots that result when we adjust the depth and width of the square cavity geometry we previously tested. We also illustrate movement of the separatrix, which is highlighted in red.
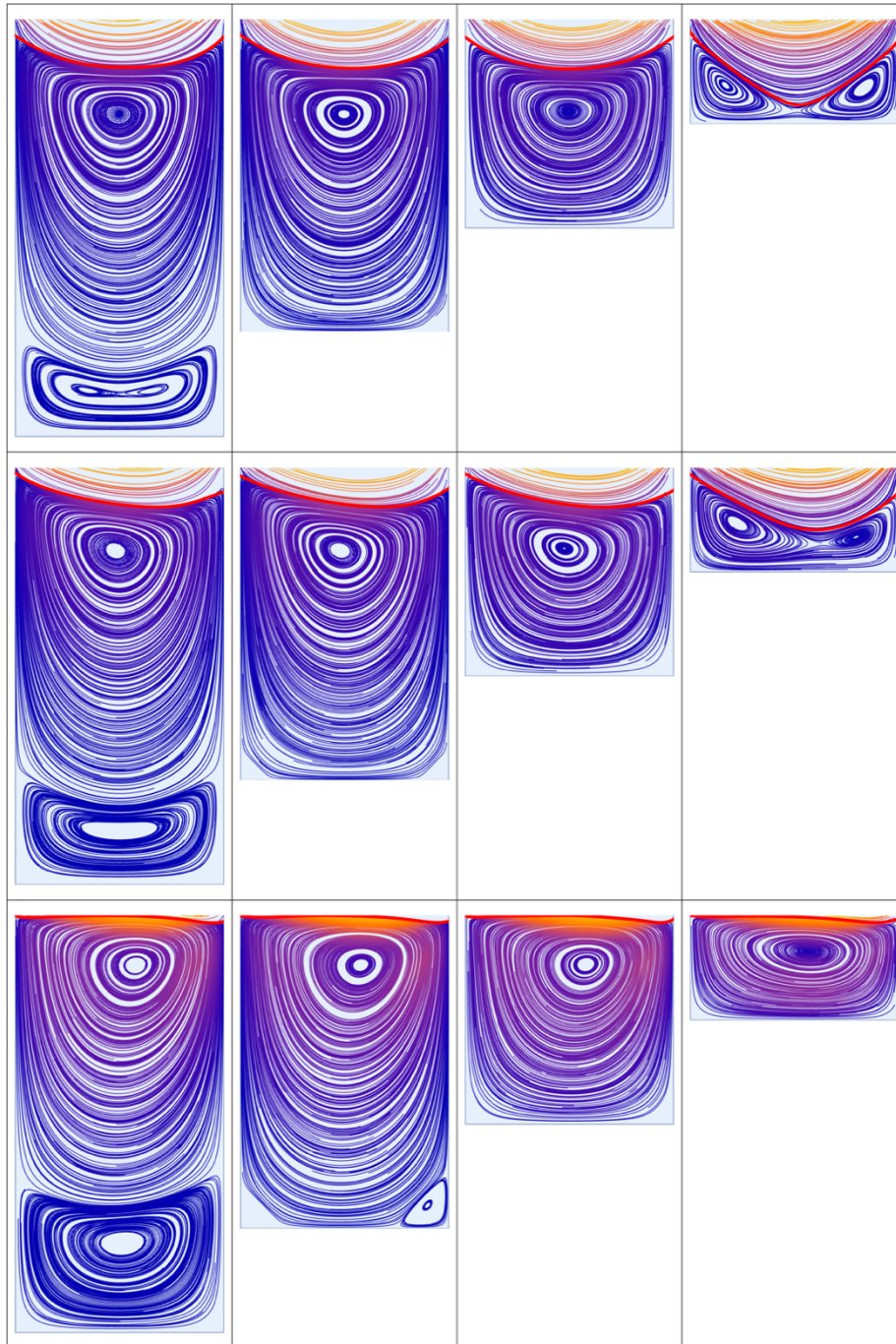
Figure 7: Stream plots for cavity depth-to-width ratios 2:1, 1.5:1, 1:1, and 0.5:1 (from left to right) and Reynolds numbers 1.81, 9.19, and 100 (from top to bottom). The separatrix location for each cavity is highlighted in red.
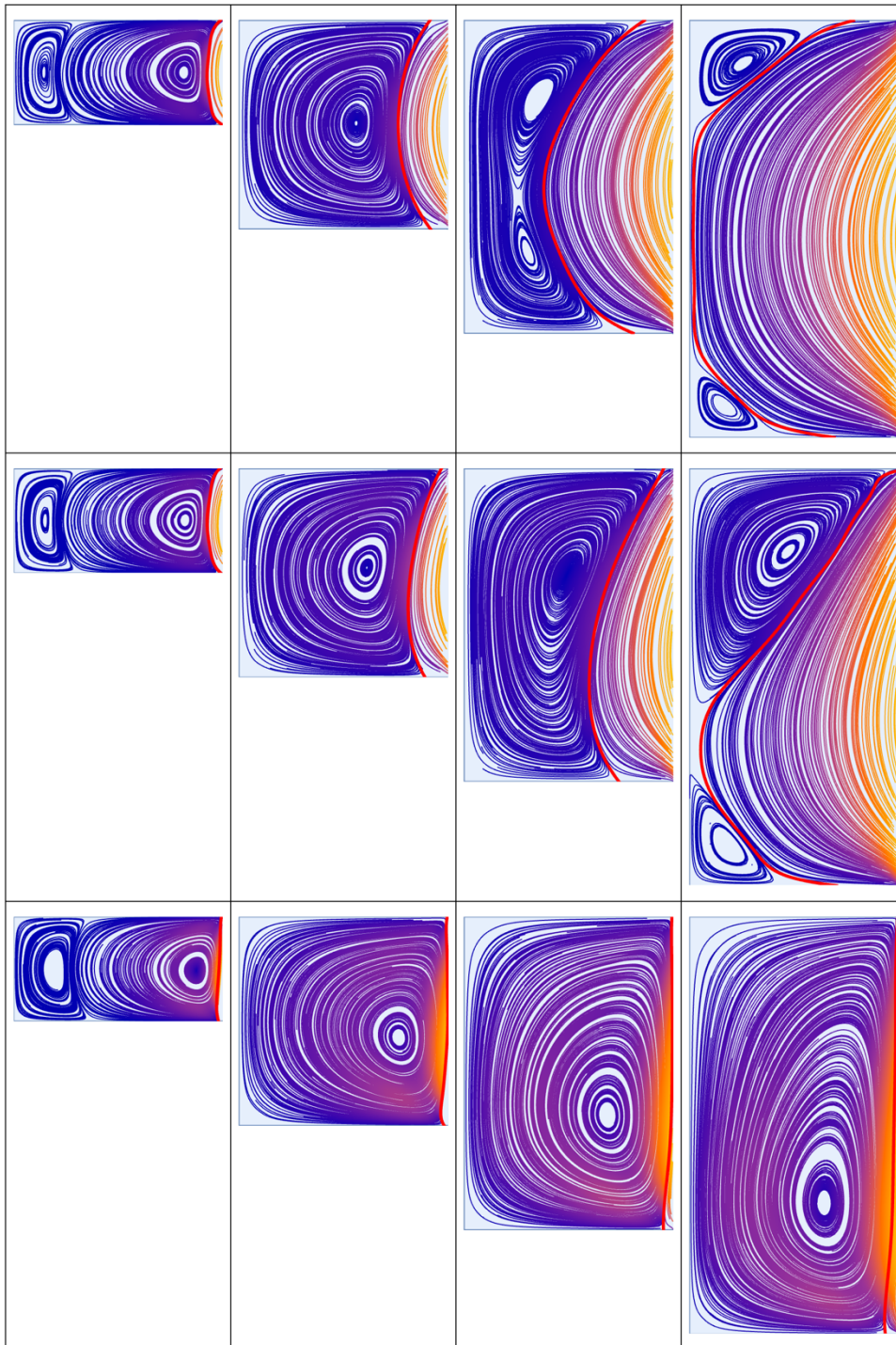
Figure 8: (as viewed in landscape orientation) Stream plots for cavity depth-to-width ratios 1:2, 1:1.5, 1:1, and 1:0.5 (from top to bottom) and Reynolds numbers 1.81, 9.19, and 100 (from left to right).

Separatrix movement, as a function of Reynolds number, is summarized in Figure 9 and 10, below. In each figure, the separatrix

140   is highlighted according to its location at a given Reynolds number (blue, yellow, green, and red for Reynolds numbers 1.81, 9.19, 50, and 100, respectively).
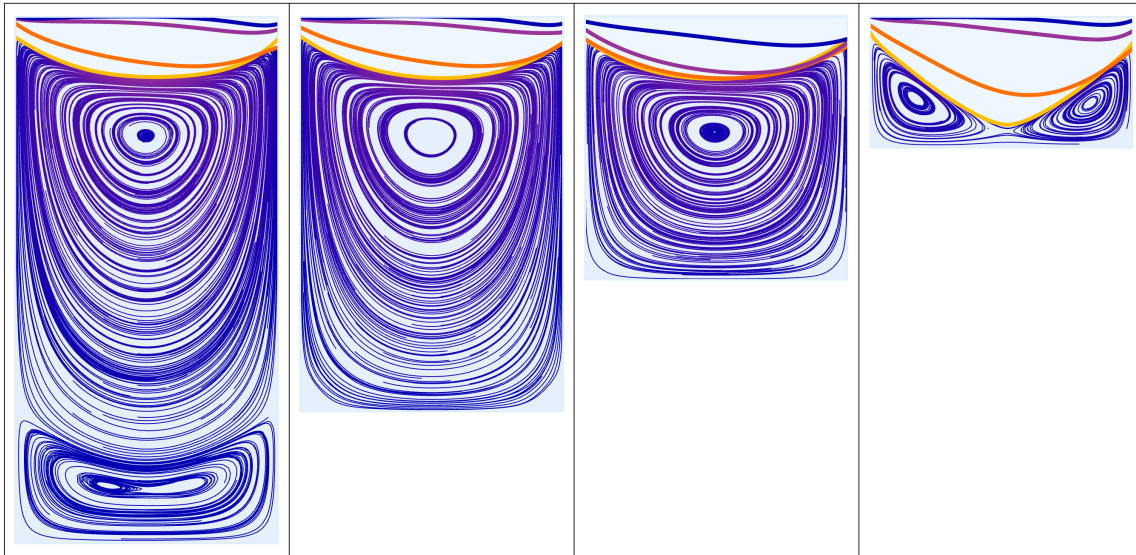
Figure 9: Separatrix locations for cavity depth-to-width ratios 2:1, 1.5:1, 1:1, and 0.5:1 (left to right) and Reynolds numbers 1.81 (blue), 9.19 (yellow), 50 (green), and 100 (red).
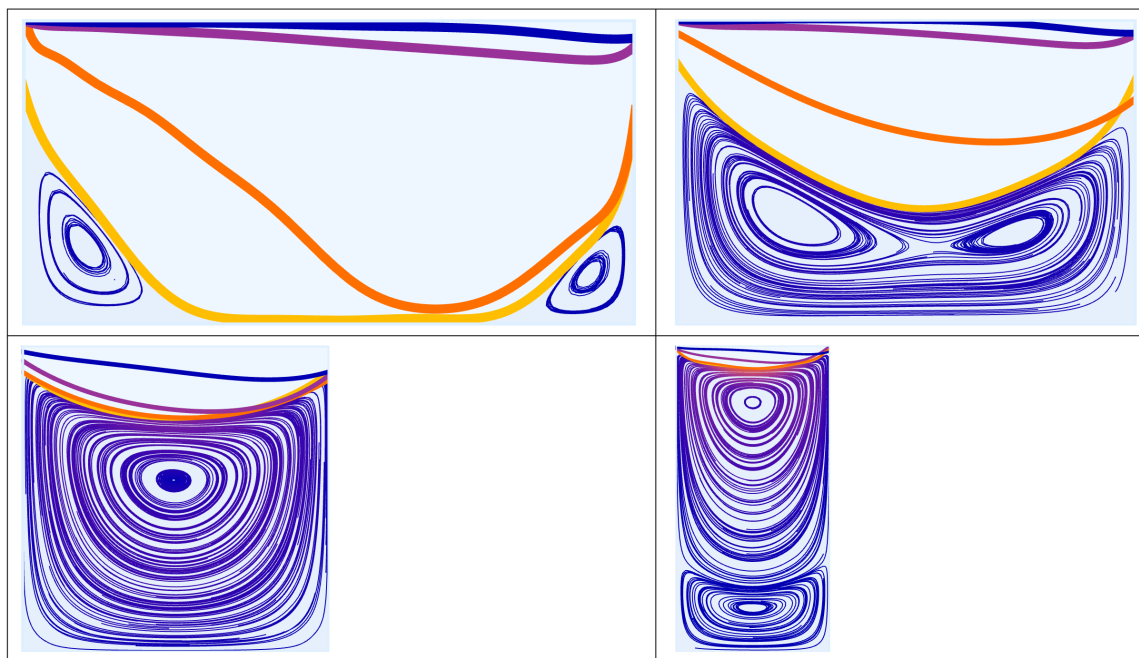
Figure 10: Separatrix locations for cavity depth-to-width ratios 1:2, 1:1.5, 1:1, and 1:0.5 (left to right) and Reynolds numbers 1.81 (blue), 9.19 (yellow), 50 (green), and 100 (red).

4.2 Separatrix Movement: Non-Rectangular Cavity Geometries

In Figure 11, we provide the stream plots for non-rectangular cavity geometries (i.e., the semicircle and equilateral triangle) with the separatrix highlighted in red.
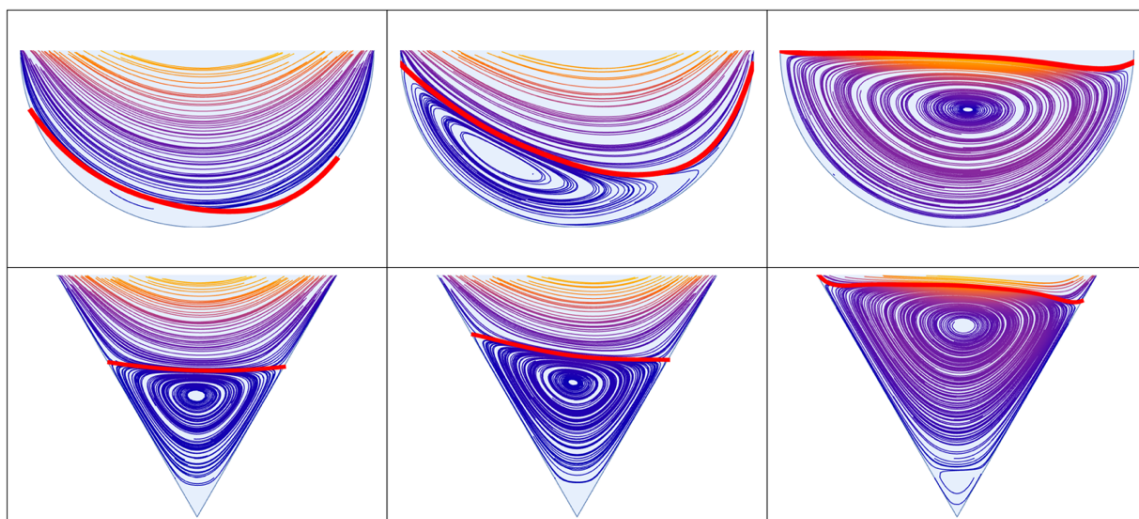
Figure 11: Stream plots for a semi-circular and triangular cavity geometry (top and bottom, respectively) for Reynolds numbers 1.81, 9.19, and 100 (from left to right) with the separatrix highlighted in red.

4.3 Separatrix Movement: Periodic Cavity Geometry

For the reader's edification, a single stream plot example of the periodic cavity flow geometry is provided below. Additional stream plots are not provided because the streamlines in each cavity are effectively identical for each of the cavity geometries pictured in Figure 12. The purpose of testing a periodic flow geometry was to determine the effect of upstream cavities on those downstream. Qualitatively, we can conclude that there is slightly less penetration of the through-flow into the downstream cavity, although this is barely evidenced by the red horizontal line in the figure below. As drawn, this line coincides with the bottom-most point of the separatrix in the upstream cavity. Note that this figure is generated for the periodic flow geometry with cavity spacing one-quarter of the cavity width, at a Reynolds number of 10.
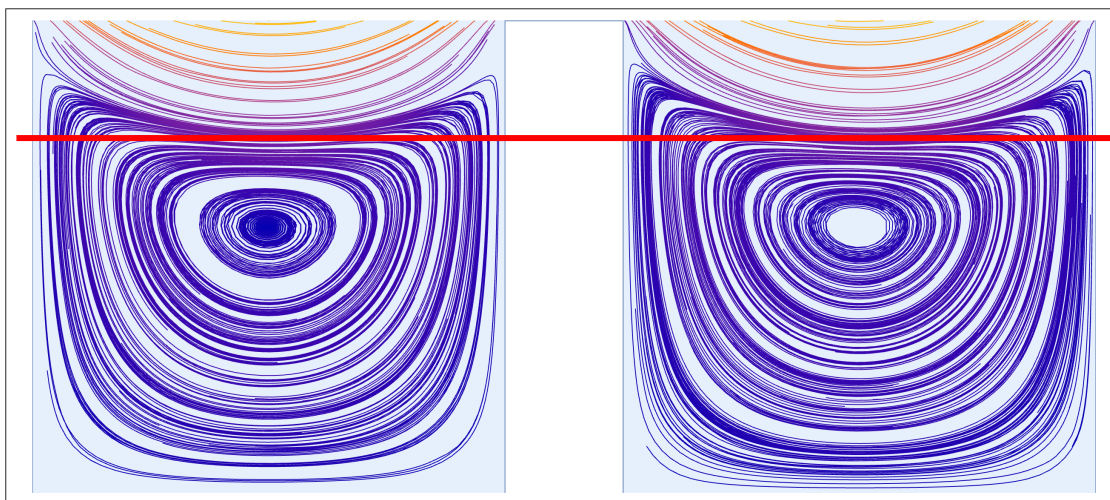
Figure 12: Stream plot of the cavities in the periodic flow geometry with a cavity spacing of one-quarter the cavity depth/width. The horizontal red line marks the bottom-most point of the separatrix of the upstream cavity (left).

4.4 Applying the Exponential Dependence of Hydrodynamic Porosity on Pore-Scale Flow Velocity

The change in hydrodynamic porosity, θ_{mobile}, as a function of Reynolds number, is provided in Figure 13 and 14, below. For ease of comparison across cavity types, we normalize θ_{mobile} by the *static* mobile-zone porosity value, θ_{MIM}, that results from enforcement of the Mobile-Immobile Zone model in the dead-end pore space. We define this quantity as:

$$\theta_{MIM} = \xi_{MIM}\,\theta \qquad (13)$$

Where ξ_{MIM} is determined by the relative magnitudes of the through-channel and cavity volumes for each dead-end pore geometry. For example, using Eq. (2), we find that for the square cavity, $\xi_{MIM} = 4/5$.

Applied to each dataset, is the exponential dependence of hydrodynamic porosity, θ_{mobile}, on pore flow velocity we previously discovered and described in Eq. (1). We remind readers that although it is the value *of the pore-space partitioning coefficient*, $\xi = \theta_{mobile}/\theta$, that we numerically quantify in this analysis, we are able to plot the hydrodynamic porosity of the medium, θ_{mobile}, because of the direct proportionality between these two quantities.
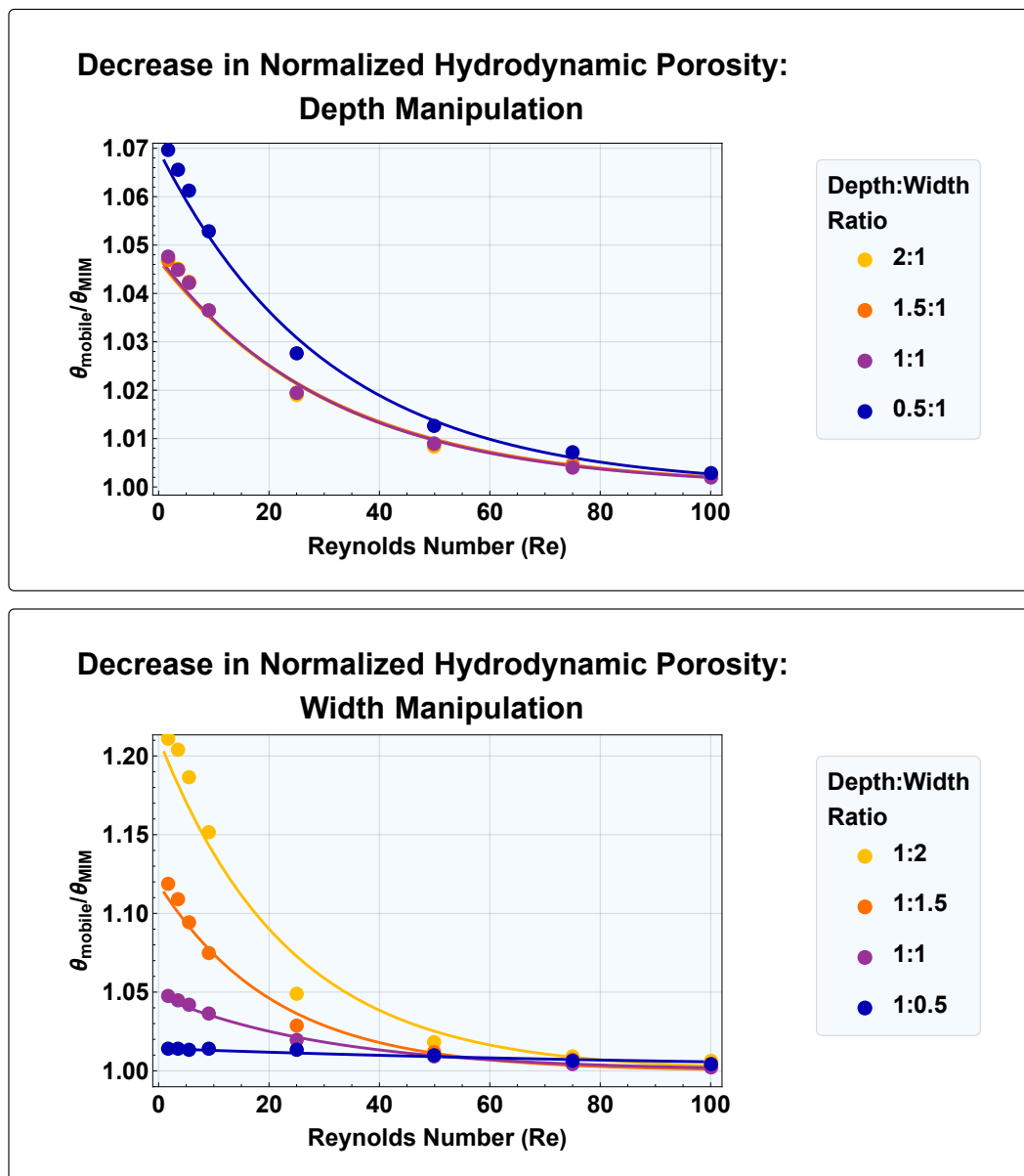
Figure 13: Normalized decrease in hydrodynamic porosity, θ_{mobile}, for media with cavity depth-to-width ratios 2:1, 1.5:1, 1:1, and 0.5:1 (top), and 1:2, 1:1.5, 1:1, and 1:0.5 (bottom).
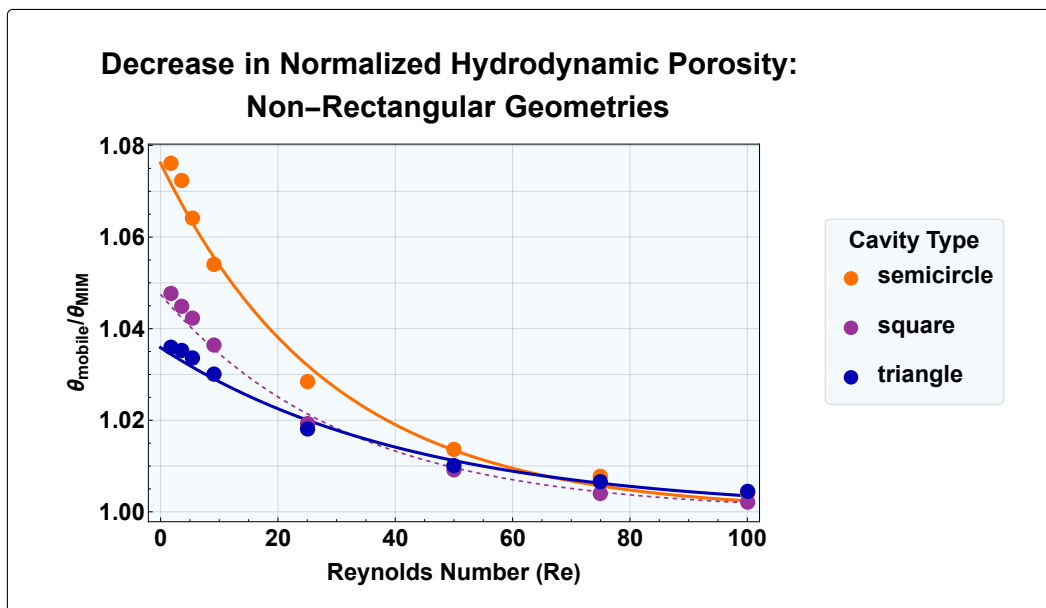
Figure 14: Normalized decrease in hydrodynamic porosity, θ_{mobile}, for media with triangular and semi-circular cavities, compared to media with square cavities.

The fitting parameters and coefficient of determination (R^2) for each model are summarized in the table below.

Table 2: Equation (1) exponential model fit parameters for each cavity geometry. Rectangular cavity geometries are specified by depth-to-width ratio.

Cavity Geometry	Equation (1) Exponential Fit Parameters			
	a	$b \times 10^2$	$c \times 10^2$	R^2
Square	0.80	3.80	3.19	0.9999
Rectangle				
2:1	0.67	3.13	3.16	0.9998
1.5:1	0.73	3.41	3.11	0.9999
0.5:1	0.89	6.19	3.26	0.9999
1:2	0.80	16.88	4.26	0.9999
1:1.5	0.80	9.50	4.73	0.9999
1:0.5	0.80	1.14	0.91	0.9999
Circle	0.91	6.94	3.47	0.9999
Triangle	0.90	3.24	2.33	0.9999

4.5 Sampling Error

Finally, the error associated with the exponential model derived from the relatively sparse dataset is approximated by fitting the exponential model to a more finely sampled dataset, pictured below. The results provided in Figure 15 are for the square cavity geometry.
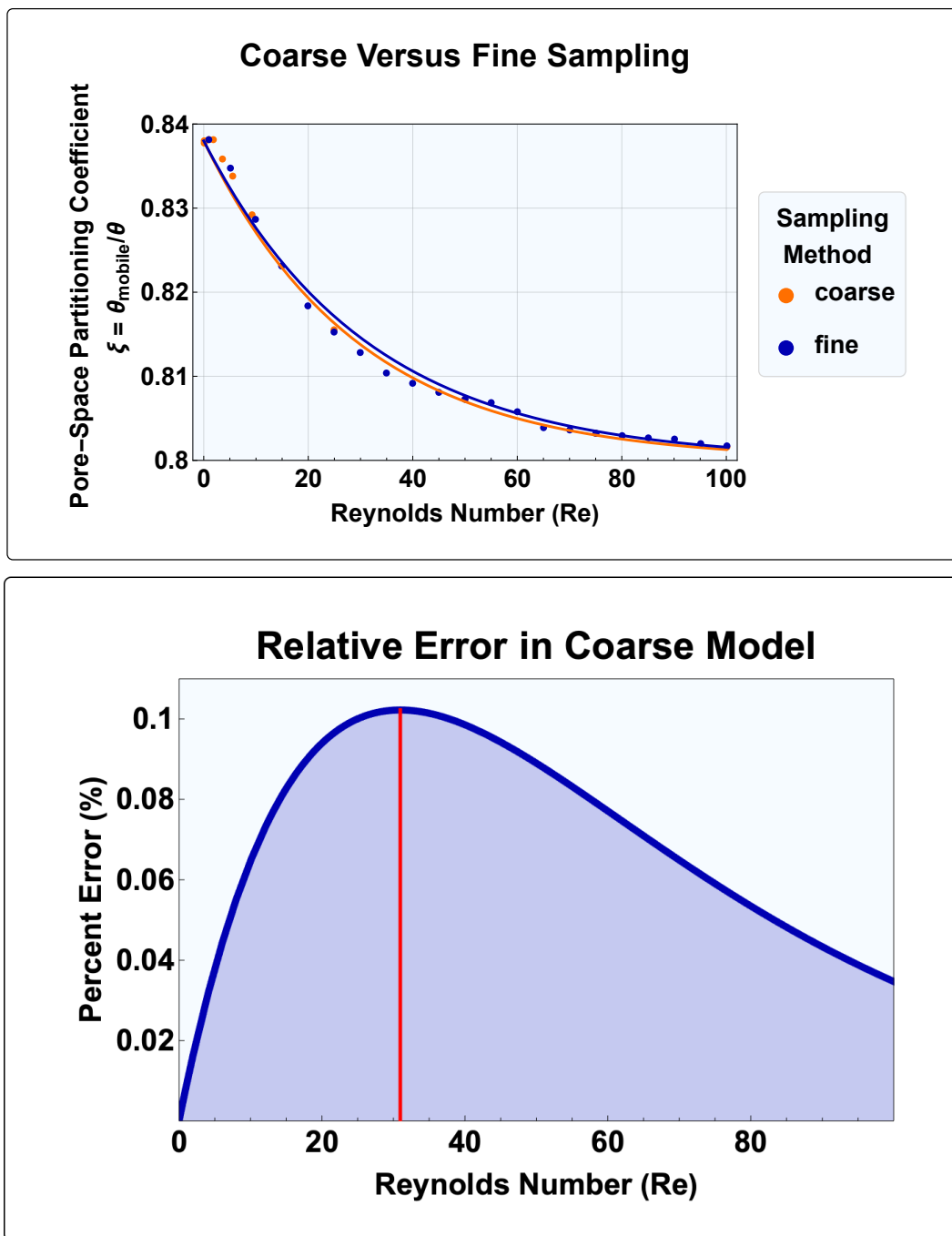
Figure 15: (top) Comparison of the exponential model that results from a sparse dataset and the exponential model that results from a more finely sampled dataset (i.e., twenty data points), and the relative error in the former (bottom).

5 Discussion

In this work, we find that the pore-space partitioning coefficient, $\xi = \theta_{mobile}/\theta$, of each of the tested cavity geometries is well-approximated by the exponential relationship in Eq. (1). In fact, the coefficient of determination (R^2) is approximately 1

205 for each dataset. Should we test additional cavity geometries in the future, given representative imaging of the pore space in an unwashed media, it would be reasonable to assume that the partitioning coefficient, and therefore the hydrodynamic porosity of that media, θ_{mobile}, would be well-approximated by this same exponential relationship. Further, our sampling frequency in the previous study did not yield a significant error in our model fit. In fact, when comparing the exponential models that result from both data sets, the largest difference between them is 0.1%. This error is an order of magnitude smaller than the error

210 associated with the measurement process, which we judge to be small enough to disregard in our analysis.

Of the tested geometries, those that exhibited the largest decrease in the pore-space partitioning coefficient, $\xi = \theta_{mobile}/\theta$, accompanying an increase in Reynolds number from 1 to 100 were rectangular. More specifically, the two largest decreases were for geometries with a cavity width greater than its depth. When the cavity width was less than its depth, however, the decrease in ξ was the smallest for all the tested geometries. In comparison, adjustment to the cavity depth did not result in such

215 large variations. Although only six rectangular cavities were tested, it appears that ξ is more sensitive to cavity width than cavity depth. Of course, this conclusion is made for a flow geometry with a through-channel height equivalent to either the cavity width or depth. Reduction of the adjacent through-channel height, as we previously demonstrated, results in more significant decreases to the mobile zone volume. These results are summarized in the table below.

Table 3: The decrease in pore-space partitioning coefficient, $\xi = \theta_{mobile}/\theta$, corresponding to an increase in channel-based Reynolds
220 **number, from 1 to 100. Rectangular cavity geometries are specified by their cavity depth-to-width ratio.**

% Decrease in Pore-Space Partitioning Coefficient, $\xi = \theta_{mobile}/\theta$	
Cavity Geometry	
Square	4.10
Rectangle	
2:1	4.05
1.5:1	4.04
0.5:1	5.91
1:2	16.09
1:1.5	9.73
1:0.5	0.81
Circle	6.45
Triangle	2.99

Further increasing the applicability of the exponential dependence of hydrodynamic porosity, θ_{mobile}, on pore-scale flow velocity, is the fact that the periodic flow geometries do not exhibit a significant difference between the upstream and downstream cavities. Given this finding, we can more confidently apply our hydrodynamic description of porosity onto a

225 periodic medium at the macroscale.

As previously mentioned, the next steps for this work are in the experimental quantification of the exponential fit parameters in Eq. (1) (i.e., *a, b*, and *c*). The ability to do so for media at sites needing remediation is necessary to demonstrate the ease with which this relationship can be tailored to a specific media. Further, it may be the case that the numerically calculated

230   parameters provided in Table 2 indicate a physical characteristic of the aggregate, effective pore geometry of real media. For example, consider the rectangular cavities with a depth-to-width ratio of 1:2 and 1:0.5. The former has a *b*-value one order of magnitude larger than the rest, and the latter, a *c*-value one order of magnitude smaller than the rest. The values in Table 2 also serve as an order of magnitude guide for what the exponential fit parameters should be in column studies.

6 Conclusions

235   In this work, we further demonstrate the applicability of the exponential dependence of hydrodynamic porosity, θ_{mobile}, on pore-scale flow velocity. We do so by testing a range of cavity geometries that are more representative of what we would expect to see in a real porous medium (i.e., rectangular, non-rectangular, and periodic geometries). Previously, we only tested a single, square cavity geometry, which is a highly idealized case. We show that not only does this exponential relationship hold for media with these new cavity geometries, but it does so almost perfectly with a coefficient of determination (R^2) of

240   approximately 1 for each set of simulation data. Given this high fit quality, it is evident that the exponential relationship we previously discovered is applicable to most, if not all, media with dead-ended pore spaces. That said, this work would lend itself well to significant expansion. Although we have highlighted sensitivity to cavity width, and previously, through-channel height to pore depth, there remain other parameters that could affect the exponential fit and perhaps, even inform us about the aggregate, effective nature of the pore spaces of experimentally studied media.

245   **Data and Code Availability**

The simulation data that support the findings of this study, and the corresponding *Mathematica* code files, are available in Open Science Framework at DOI 10.17605/OSF.IO/P2EMN. All files are also provided in pdf format for readers that do not have access to *Mathematica*.

Author Contributions Statement

250   Conceptualization (Z.J.K.), data curation (A.H.Y.), formal analysis (A.H.Y.), investigation (A.H.Y. and. Z.J.K.), methodology (A.H.Y. and. Z.J.K.), project administration (Z.J.K.), supervision (Z.J.K.), validation (A.H.Y.), visualization (A.H.Y.), writing – original draft (A.H.Y. and. Z.J.K.), writing – review & editing (A.H.Y. and. Z.J.K.).

Declaration Of Competing Interest

The authors declare no competing conflict of interest.

255 **Acknowledgements**

This work is, in part, supported by a grant, OPP1173370 (Sanitation Technology Cluster), from the Bill & Melinda Gates Foundation through Duke University's Center for WaSH-AID. All opinions, findings, and conclusions or recommendations expressed in these works are those of the author(s) and do not necessarily reflect the views of the Foundation, Duke, or the Center.

260

References

Alkire, R. C., Deligianni, H., and Ju, J. B.: Effect of Fluid-Flow on Convective-Transport in Small Cavities, J. Electrochem. Soc., 137, 818-824, https://doi.org/10.1149/1.2086562, 1990.

Bu, S., Yang, J., Dong, Q., and Wang, Q.: Experimental Study of Transition Flow in Packed Beds of Spheres with Different Particle Sizes Based on Electrochemical Microelectrodes Measurement, Appl. Therm. Eng., 73, 1525-1532, https://doi.org/10.1016/j.applthermaleng.2014.03.063, 2014.

Elderkin, R. H.: Separatrix Structure for Elliptic Flows, Am. J. Math., 97, 221-247, https://doi.org/10.2307/2373669, 1975.

Fang, L. C., Cleaver, J. W., and Nicolaou, D.: Hydrodynamic Cleansing of Cavities, 8th International Conference on Computational Methods and Experimental Measurements (CMEM 97), Rhodes, Greece, May, WOS:A1997BJ12J00038, 391-401, 1997.

Higdon, J. J. L.: Stokes Flow in Arbitrary Two-Dimensional Domains: Shear Flow over Ridges and Cavities, J. Fluid Mech., 159, https://doi.org/10.1017/s0022112085003172, 1985.

Horner, M., Metcalfe, G. U. Y., Wiggins, S., and Ottino, J. M.: Transport Enhancement Mechanisms in Open Cavities, J. Fluid Mech., 452, 199-229, https://doi.org/10.1017/s0022112001006917, 2002.

Jolls, K. R. and Hanratty, T. J.: Transition to Turbulence for Flow through a Dumped Bed of Spheres, Chem. Eng. Sci., 21, 1185-&, https://doi.org/10.1016/0009-2509(66)85038-8, 1966.

Kahler, D. M. and Kabala, Z. J.: Acceleration of Groundwater Remediation by Deep Sweeps and Vortex Ejections Induced by Rapidly Pulsed Pumping, Water Resour. Res., 52, 3930-3940, https://doi.org/10.1002/2015wr017157, 2016.

Kang, I. S. and Chang, H. N.: The Effect of Turbulence Promoters on Mass-Transfer - Numerical-Analysis and Flow Visualization, Int. J. Heat Mass Tran., 25, 1167-1181, https://doi.org/10.1016/0017-9310(82)90211-3, 1982.

Latifi, M. A., Midoux, N., Storck, A., and Gence, J. N.: The Use of Micro-Electrodes in the Study of the Flow Regimes in a Packed-Bed Reactor with Single-Phase Liquid Flow, Chem. Eng. Sci., 44, 2501-2508, https://doi.org/0.1016/0009-2509(89)85194-2, 1989.

Mehta, U. B. and Lavan, Z.: Flow in a Two-Dimensional Channel with a Rectangular Cavity, J. Appl. Mech., 36, 897, https://doi.org/10.1115/1.3564799, 1969.

Moffatt, H. K.: Viscous and Resistive Eddies near a Sharp Corner, J. Fluid Mech., 18, 1-18, https://doi.org/10.1017/s0022112064000015, 1963.

O' Brien, V.: Closed Streamlines Associated with Channel Flow over a Cavity, Phys. Fluids, 15, https://doi.org/10.1063/1.1693840, 1972.

O'Neill, M. E.: Separation of a Slow Linear Shear-Flow from a Cylindrical Ridge or Trough in a Plane, Z. Angew. Math Phys., 28, 439-448, https://doi.org/10.1007/bf01601625, 1977.

Rode, S., Midoux, N., Latifi, M. A., Storck, A., and Saatdjian, E.: Hydrodynamics of Liquid Flow in Packed Beds: An Experimental Study Using Electrochemical Shear Rate Sensors, Chem. Eng. Sci., 49, 889-900, https://doi.org/10.1016/0009-2509(94)80025-1, 1994.

295   Shankar, P. N. and Deshpande, M. D.: Fluid Mechanics in the Driven Cavity, Annu. Rev. Fluid Mech., 32, 93-136, https://doi.org/10.1146/annurev.fluid.32.1.93, 2000.

Shen, C. and Floryan, J. M.: Low Reynolds Number Flow over Cavities, Phys. Fluids, 28, https://doi.org/10.1063/1.865366, 1985.

Vangenuchten, M. T. and Wierenga, P. J.: Mass-Transfer Studies in Sorbing Porous-Media .1. Analytical Solutions, Soil Sci.
300   Soc. Am. J., 40, 473-480, https://doi.org/10.2136/sssaj1976.03615995004000040011x, 1976.

Wegner, T. H., Karabelas, A. J., and Hanratty, T. J.: Visual Studies of Flow in a Regular Array of Spheres, Chem. Eng. Sci., 26, https://doi.org/10.1016/0009-2509(71)86081-5, 1971.

Weiss, J. B.: Transport and Mixing in Traveling Waves, Phys. Fluids A-Fluid., 3, 1379-1384, https://doi.org/10.1063/1.858068, 1991.

305   Young, A. H. and Kabala, Z. J.: *(under Review)* Hydrodynamic Porosity: A Paradigm Shift in Flow in Porous Media, Part I, Hydrol. Earth Syst. Sc., 2023.